nature portfolio

https://doi.org/10.1038/s41551-021-00723-y

Supplementary information

Miniaturized electromechanical devices for the characterization of the biomechanics of deep tissue

In the format provided by the
authors and unedited

Table of Contents

Supplementary Note 1:

Finite Element Analysis (FEA). The commercial software ABAQUS was used to study the mechanical interaction among the actuator, Au gauge and tissues to be measured. The PDMS, phantom tissues and magnet were modeled by hexahedron elements (C3D8R) while the thin Au and Polyimide film were modeled by composite shell elements (S4R). The minimal element size was 1/5 of the width of the narrowest interconnects (50 μm). The mesh convergence of the simulation was ensured for all cases. The elastic modulus (E), Poisson's ratio (v) and density (ρ) are E_{PDMS}=1MPa, v_{PDMS} =0.5, ρ_{PDMS}= 0.96×10^3 kg/m^3, E_{Au}=79 GPa, v_{Au} =0.4, ρ_{Au}=19.32×10^3 kg/m^3, E_{magnet}=113 GPa, v_{magnet}=0.34, and ρ_{magnet}=8.08×10^3 kg/m^3, E_{PI}=2.5 GPa, v_{PI}=0.34, ρ_{PI}=0.91×10^3 kg/m^3, E_{Cu}=119 GPa, v_{Cu}=0.32, and ρ_{Cu}=8.96×10^3 kg/m^3.

Wireless and Fully-wearable Design. For the purpose of daily monitoring without benchtop lock-in detection system, Supplementary Fig. 28 presents a compact device design that integrates EMM sensing into wearable, skin-integrated platforms via wireless control in terms of recent publication (1). Here, a power management module includes a booster, a regulator and a current source, as a power supply to drive actuator vibration as well as EMM sensing. A band-pass filter can thus yield the voltage response (V_S) at a certain frequency, for subsequent amplification by as much as 100 times (up to ~10 mV) within a signal processing module. This setup can replace the lock-in electronics. A microcontroller unit (MCU) with integrated Bluetooth low energy (BLE) function (TI CC2640R2F) can support data sampling and wireless data transmission for direct delivery and simultaneous conversion into modulus values on a customized device (*i.e.* a smart phone). The overall system can be fabricated on a flexible printed circuit board (PCB, 3 × 3 cm^2, ~1 mm thick), as the basis for a wearable platform that includes not only actuating/sensing components but also a data-collection terminal. Future work will focus on realization of this design as well as battery-free alternatives (2).

Time-domain Signal Measurement during Actuation. The time domain signals of the EMM sensor were acquired by a data acquisition system (DAQ, PowerLab 16/35, AD Instruments) and a matched amplifier (FE132 Bio Amp, AD Instruments), as shown in Supplementary Fig. 14. For a given actuation frequency (~50 Hz), variations of gauge resistance (typically as ~0.05 Ohm) produce a signal upon application of a constant current I_S (1 mA). Such signal (narrow band-pass filtered) gradually becomes stable in accordance to same frequency with a settling duration of ~0.3 s across the ring-down time (blue region in Supplementary Fig. 15a), and then yields a level of voltage amplitude of ~35 μV continuously on artificial skin (500 kPa, 3 mm thick), as the final V_S that can be extracted via lock-in technique. By comparison, increasing tissue thickness and decreasing tissue modulus can lead to increases of V_S (Supplementary Fig. 15b), consistent with results of Figs. 2f, 2g, while settling time still remains low(< 0.4 s) for all these cases, indicating rapid, precise measurements of the sensor on different tissues.

Electromagnetic induction effect. During the measurement, alternating currents through the top coil of the actuator can induce an electromagnetic induction effect associated with the metal traces that define the strain gauge and the flower-shape mesh structure, thereby resulting in additional output voltage. To facilitate measurement of this induction effect, the magnet was removed from actuator during V_A input into the top coil. As shown in Supplementary Fig. 16, the induced output voltages were separately measured as a function of actuation frequencies (10-10,000 Hz), while the EMM sensor without the magnet couples onto a sample of artificial skin with elastic modulus of 200 kPa. The induced voltages remained below ~0.5 μV at low frequency (below 100 Hz), which were ~2 orders of magnitude lower than the signals. This effect increased with increasing actuation frequency, with an output voltage higher than 10 μV at 1000 Hz.

Operation for Multiplexed Arrays of EMM Sensors. Fabrication of multiple strain gauges and repetitive transfer-printing onto a large-area layer of PDMS form an array of gauges (Supplementary Fig. 32) and electronic interconnects based on flexible, lightweight conductive cables (heat seal connectors (HSCs), Elform Inc.). Connection to an external multiplexing board allow for an interface to a 4:1 multiplexer that enables readout from each gauge at a time, as controlled via a back-end DAQ system. Assemblies of actuators aligned with the strain gauge array yielded the complete mapping systems (Supplementary Fig. 33).

Operation of the multiplexed array of EMM sensors appears in Supplementary Fig. 34. During measurements, all of the actuators are connected for vibration at a specific frequency (*f*) and amplitude of input voltage. The setup for spatial mapping of the skin modulus used a function generator (Tektronix) to produce a sine-wave power input with preprogrammed frequency and amplitude, delivered through the interface board to certain actuators in the mapping system. For the strain gauge array, a current source connected through the interface board to a multiplexer delivered current to a certain gauge in the system. A lock-in amplifier (SR830, Stanford Research) connected through the interface board to a demultiplexer captured the corresponding change in voltage, to yield the elastic modulus at the corresponding location. Here, the multiplexers modulated by the controller enabled continuous scanning of the arrays of the EMM sensors at a sampling rate 5 Hz. With a constant current delivered from the current source (Keithley 6221, Tektronix) to the strain gauge, the lock-in amplifier (SRS SR830, Stanford Research) captured the amplitude of fluctuations in the resistance of the strain gauge by measuring the sensing voltage at certain frequencies.

References

1. Yu, X. et al. Skin-integrated wireless haptic interfaces for virtual and augmented reality. *Nature* **575**, 473-479 (2019).

2. P. Gutruf et al. Wireless, Battery-free, Fully Implantable Multimodal and Multisite Pacemakers for Applications in Small Animal Models. *Nat. Commun.* **10**, 5742 (2019).

Supplementary Figure Legends

Figure S1. Steps for fabricating and assembling EMM sensors. 1. Formation of electrical interconnects and strain gauges on glass wafers; 2. Transfer-printing procedure with a water soluble tape; 3. Printing onto a flexible layer of PDMS; 4. Assembly of the gauge with mechanical actuators, connected via wires and a PCB.

Figure S2. Schematic cross-sectional illustration in sequence for device fabrication, including both (a) transfer printing and (b) assembly process. Here, PI stands for polyimide and RIE corresponds to reactive ion etching.

Figure S3. The strain gauge consisting of two-terminal Au wire connection embedded in polyimide layer, with (**a**) circuit diagram and (**b**, **c**) optical images of different locations.

Figure S4. Measurement setup for mechanical sensing. (**a**) Photograph of setup includes a current source, a lock-in amplifier and EMM sensor with external connection and biological measurement targets. (**b**) Schematic illustration for operational mechanism.

Figure S5. Robust mechanical properties of devices. (a) The flexible sheet of strain gauges during twisted. (b) The entire system laminated onto a curved surface. (c) Device signals in terms of various adhesion conditions with different weight ratios of crosslinker in PDMS and after 500× cycles of use.

Figure S6. (**a**) Gauge resistance as a function of cycles of bending. Inset is an optical image of the gauge on a surface with a radius of curvature of 1.5 cm. (**b**) Statistics of resistance changes of gauge in an individual bending with different bending radii. (**c**) Bending tests and accelerated soak tests of the strain gauge. Inset shows an image of a gauge immersed in artificial sweat at 50 ^{o}C.

Figure S7. Systematic studies of the bending effects of EMM sensor measurements. (a) EMM sensors coupled on cylindrical substrates of PDMS with radius of curvature of 4 cm, 8 cm, 10 cm and ∞ cm, respectively. (b) EMM sensors coupled on substrates with overlarge curvature with bending radius of 2 cm. Delamination occurs at the contact surface. (c) Signals of EMM sensors with different bending radii.

Figure S8. Statistics on the resistance (strain gauge), yield, and the *SNR* (during measurements on cheek) of 100 fabricated devices. The yield corresponds to the percentage of functional devices.

Figure S9. Applications of EMM sensors on human subjects. The system can be placed in contact with various locations of human body such as the (**a**) forearm and (**b**) shoulder. An adhesive film (3M Tegaderm Film) laminated on top of the entire structure prevents motion during measurements.

Figure S10. Normalized amplitude-frequency response of the vibratory actuator in contact with an artificial skin sample with an modulus of 200 kPa.

Figure S11. (**a**) Schematic diagram of an EMM sensor coupled onto artificial skin samples (PDMS layers) on glass substrates, as an approximate mimic of the structure of device/skin/bones. (**b**) A collection of measurements of elastic modulus on different PDMS layers, as function of weight ratios of crosslinker, all tested by the commercial bio-indenter.

Figure S12. Measurements for force generated by the actuator. (**a**) Experimental setup for the force measurement, with a flexible force sensor placed between PDMS and actuator. (**b**, **c**, **d**) The generated force by magnet impact on (b) 1 mm-, (c) 2 mm- and (d) 3 mm-thick artificial skin (200 kPa).

Figure S13. Strategies to increase the force on measurement targets. (a) Comparative results of the forces generated by applying different additional DC bias. (b) Generated force by sine-wave and square-wave input voltage with the same amplitude (5 V).

Figure S14. Photograph for the measurement setup to record the time signal of sensor.

Figure S15. Time signals of sensor on different artificial skins. (**a**) Signal measured on tissue-phantom model (PDMS, 1mm thick, 500 kPa) as a function of actuation time, with amplitude variations < 5% and settling time of ~0.3 s. (**b**) Amplitudes of signal and settling time measured on different types of samples with various thicknesses and moduli, measured among 10 devices.

Figure S16. Recording of sensing voltages of V_S as function of actuation frequencies on artificial skin samples with elastic moduli of 200 kPa, without the magnets.

Figure S17. (**a**) Schematic illustration for two device structures, with coil contacting on strain gauge and the original construct in Fig. 1a. (**b**) Induced voltages by electromagnetic induction effect in EMM sensor as a function of actuation frequencies, in different designs.

Figure S18. Simulated (line) and measured (symbols) V_S as a function of elastic modulus of the PDMS sample at 50 Hz, with constant thickness of 8 mm.

Figure S19. Results of experimental (E), FEA results and the fitting lines (Equation 1) of V_S as a function of sample thicknesses with various sample moduli.

Figure S20. Mechanical evaluation of *ex-vivo* porcine skin via DMA techniques. (**a**)-(**e**) Stress-strain responses of the porcine skin with different hydration level tested by DMA in quasi-static strain rate regimes, with different modulus values. (**f**) Comparative modulus results from EMM sensor (red) and from DMA methods (blue).

Figure S21. Summarized modulus measurements of tissue-phantom model, porcine skin and muscles via different methods, with inset of photograph of measurement on porcine muscle. Inset shows the photograph of measurement with EMM sensor on porcine muscle (5 cm thick).

Figure S22. Comparison of measurement results with EMM sensors on the same location of a human thigh with (**a**) hair bearing and (**b**) hairless regions. (**c**) The output sensing voltages show stable performance on both regions.

Figure S23. Measurement results at different body sites. (**a**) Photograph of measurement on finger joint. (**b**) Signals obtained at the sites in (a) and at belly region of a volunteer subject.

Figure S24. Comparative results of signals with device measurements on different locations of human body between lean subjects (red) and overweight (blue) subjects. To expand the signal variation, devices were mounted on test region with underlying muscle stressed during all measurements. Error bars correspond to the standard deviation for measurements among volunteer subjects.

Figure S25. Measurements of various muscle states. (**a,b,c**) Photographs of devices coupled on thigh region of a volunteer subject during muscle states of (a) standing, (b) sitting and (c) lying (from left to right). (**d**) Measurement signals for different muscle states.

Figure S26. Schematic illustration of a simulated patient test. EMM sensors are coupled onto a silicone substrate (1 cm thick), with modulus of 500 kPa for the central part (1 cm diameter) and of 100 kPa for the surrounding part of the substrate that mimics the structure of a skin tumor, in an exploded (**a**) and cross-sectional (**b**) view. (**c**) Measurement results of the simulated patient test. Left: Photograph of the simulated test. Right: EMM measurements of modulus values at the central and surrounding regions of the silicone substrate.

Figure S27. EMM measurements on (**a**) arm (**c**) hand and (**e**) lower back, with sensors on psoriasis lesion (right) and on nearby skin under normal conditions (left). Black frames correspond to the lesion regions of psoriasis. (**b**), (**d**), (**f**) Measurement results for the modulus values of lesions and nearby normal skin, collected in (**a**), (**c**) and (**e**). Error bars correspond to standard deviation for multiple measurements within a same subject.

Figure S28. Schematic diagram of a feasible fully-wearable system under wireless control.

Figure S29. Experimental results for sensing voltages from EMM sensors with (**a**) 3 mm diameter and (**b**) 1.5 mm diameter magnets as function of the thickness of artificial skin samples.

Figure S30. FEA modeling to determine the modulus of skin and inner tissues for (**a**) cheek region and (**b**) fingertip dorsum from measurements using EMM sensors with different D. Here, E_A and E_B correspond to elastic modulus for skin and inner tissues. Insets show the photographs of the measurements.

Figure S31. Simple estimation of tissue thickness in fingertip dorsum, with length measurements (**a**) from bottom of fingertip to nail plate; and (**b**) from bottom of fingertip to fingertip dorsum near the nail plate. The combined thickness for skin/tissues of fingertip dorsum near the nail root is ~3 mm.

Figure S32. Photograph of the strain gauge array on a polymer substrate during bent status.

Figure S33. (**a**) Photograph of the final, complete EMM mapping array laminated on an artificial skin (PDMS, 2 cm thick). Interconnections use flexible cable of heat seal connectors (HSCs). (**b**) The connection of the EMM array system to an external multiplexing board.

Figure S34. Schematic illustration of the DAQ system.

Table S1. The relationship between the elastic modulus E of tissues and $C(E)$ in Equation (1).

Table S2. Summary of specific diseases and corresponding tissue mechanics. All values reported can be found in the corresponding references[20,21,50-52].

Movie S1. The video captured using a high-speed camera for vibration of magnet in slow motion at 50 Hz and V_A of 5 V.

Movie S2. Visualization of magnet vibration in slow motion at 50 Hz on the artificial skin (PDMS, 200 kPa, 3 mm thick), with a travelling amplitude of ~300 μm.

Figure S1

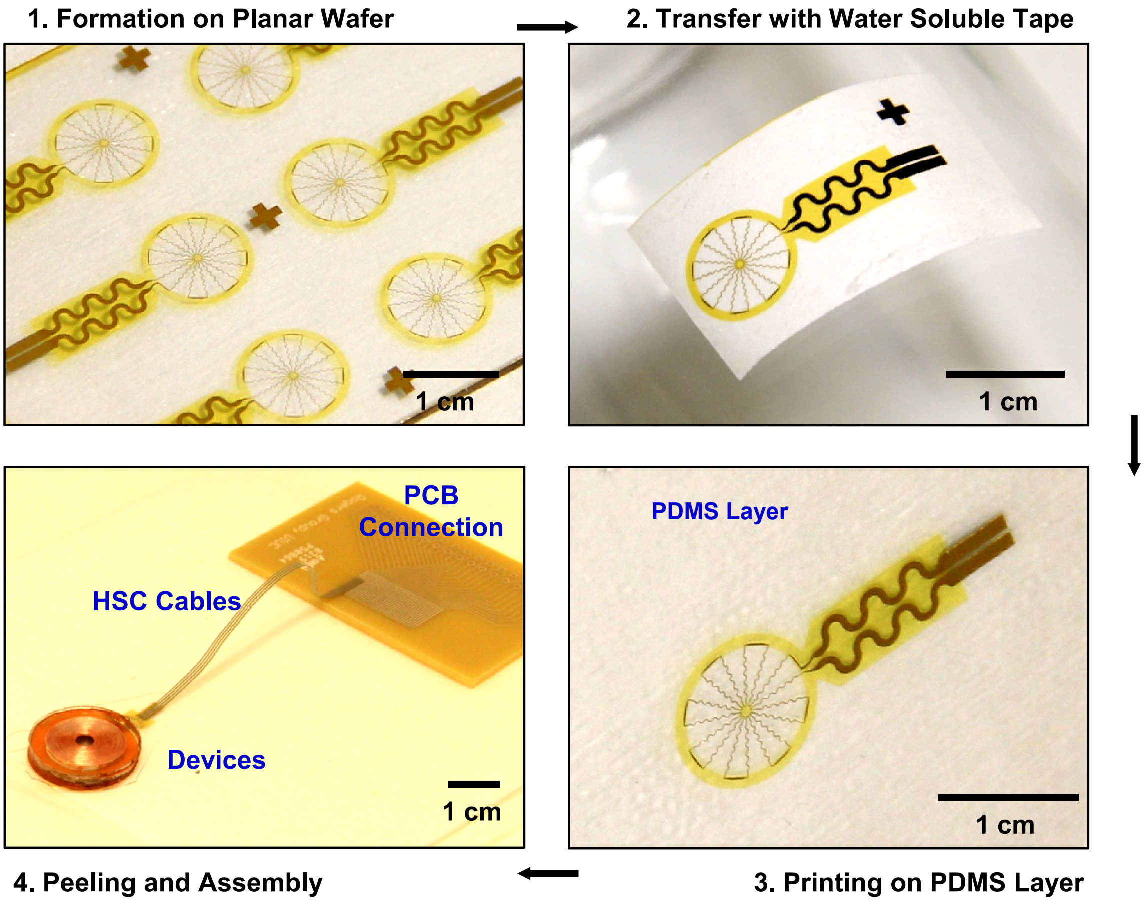

Figure S1. Steps for fabricating and assembling EMM sensors. 1. Formation of electrical interconnects and strain gauges on glass wafers; 2. Transfer-printing procedure with a water soluble tape; 3. Printing onto a flexible layer of PDMS; 4. Assembly of the gauge with mechanical actuators, connected via wires and a PCB.

Figure S2

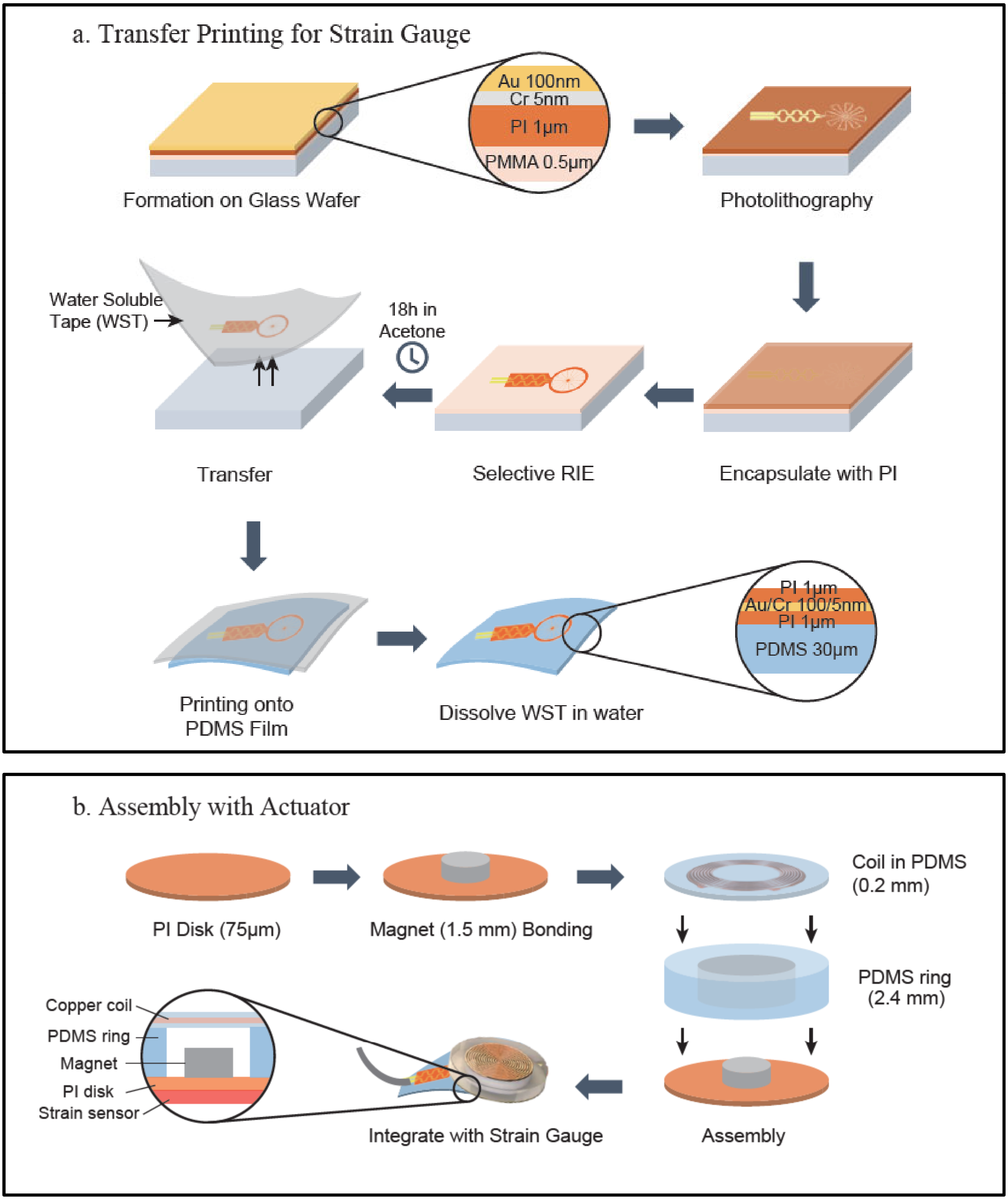

Figure S2. Schematic cross-sectional illustration in sequence for device fabrication, including both (a) transfer printing and (b) assembly process. Here, PI stands for polyimide and RIE corresponds to reactive ion etching.

Figure S3

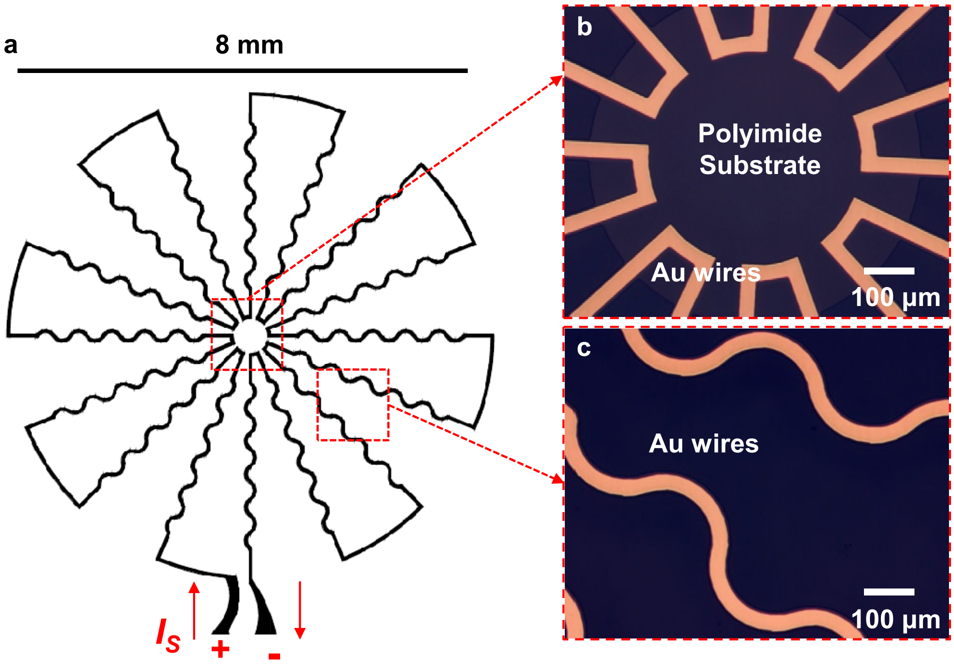

Figure S3. The strain gauge consisting of two-terminal Au wire connection embedded in polyimide layer, with (**a**) circuit diagram and (**b**, **c**) optical images of different locations.

Figure S4

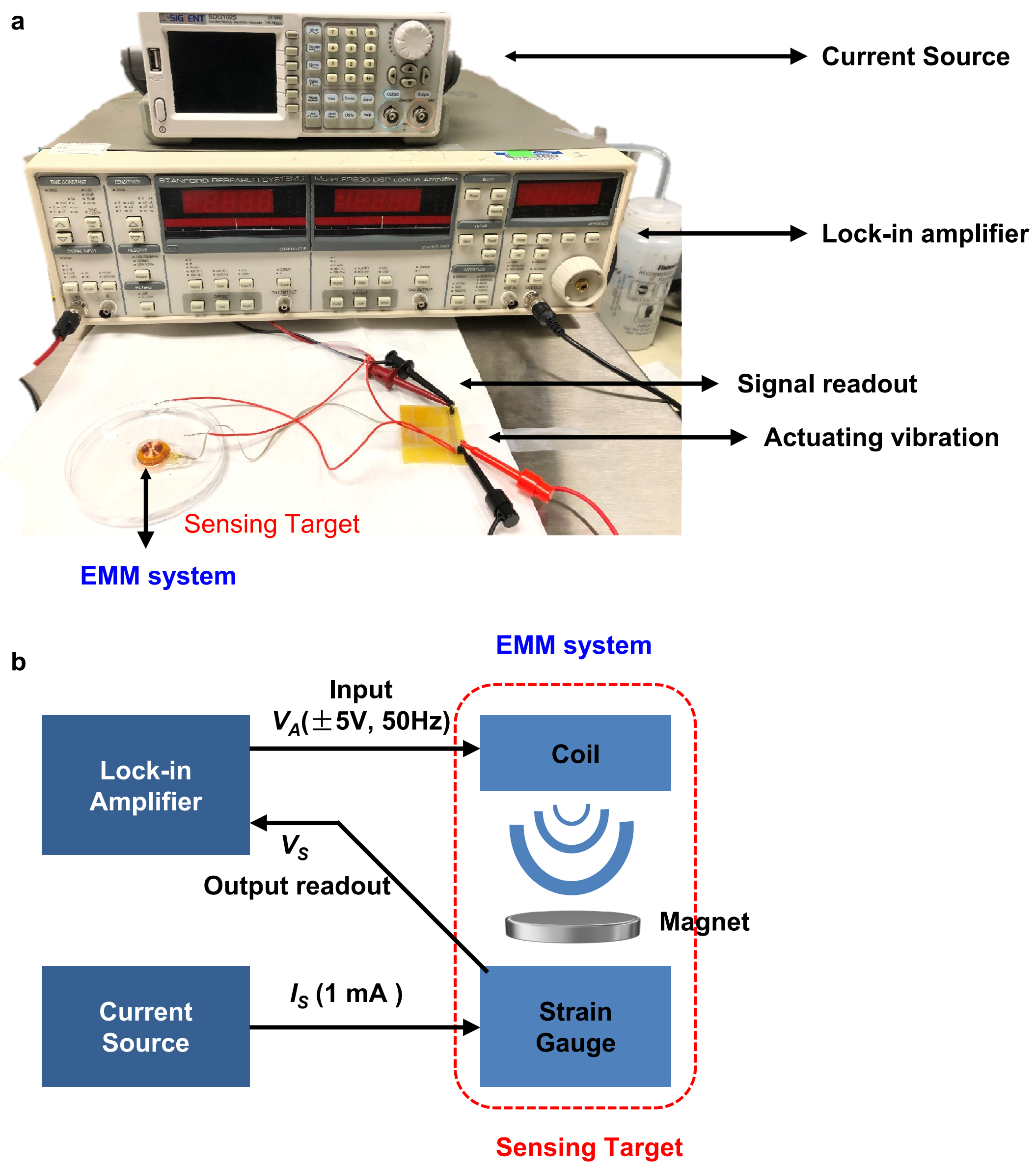

Figure S4. Measurement setup for mechanical sensing. (**a**) Photograph of setup includes a current source, a lock-in amplifier and EMM sensor with external connection and biological measurement targets. (**b**) Schematic illustration for operational mechanism.

Figure S5

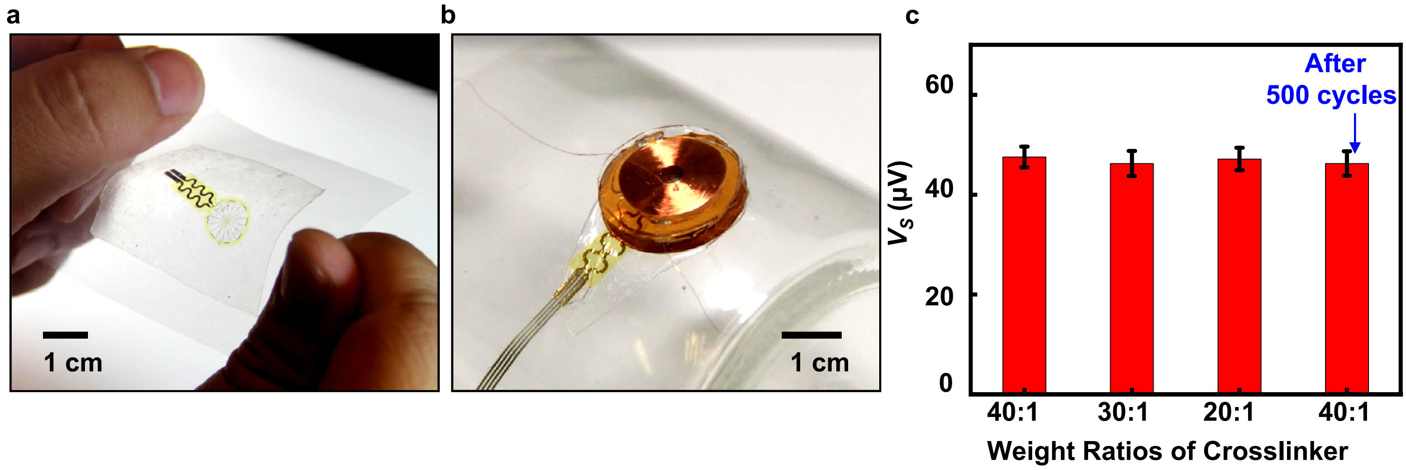

Figure S5. Robust mechanical properties of devices. (a) The flexible sheet of strain gauges during twisted. (b) The entire system laminated onto a curved surface. (c) Device signals in terms of various adhesion conditions with different weight ratios of crosslinker in PDMS and after 500× cycles of use. Error bars correspond to the standard deviation for multiple measurements with five different devices in each case.

Figure S6

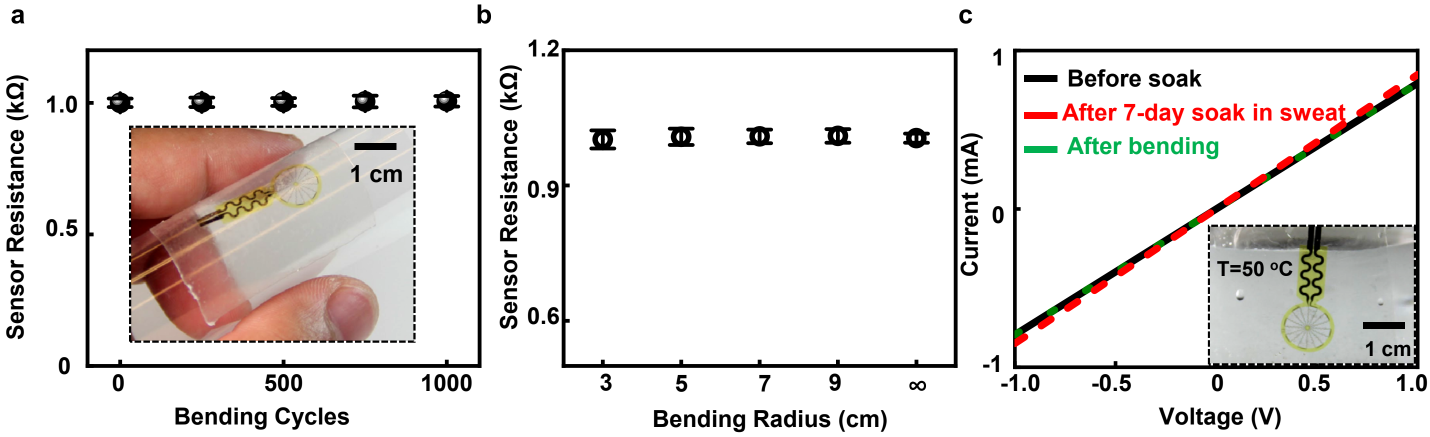

Figure S6. (**a**) Gauge resistance as a function of cycles of bending. Inset is an optical image of the gauge on a surface with a radius of curvature of 1.5 cm. (**b**) Statistics of resistance changes of gauge in an individual bending with different bending radii. Error bars correspond to the standard deviation for measurements with 10 different devices. (**c**) Bending tests and accelerated soak tests of the strain gauge. Inset shows an image of a gauge immersed in artificial sweat at 50 ^{o}C.

Figure S7

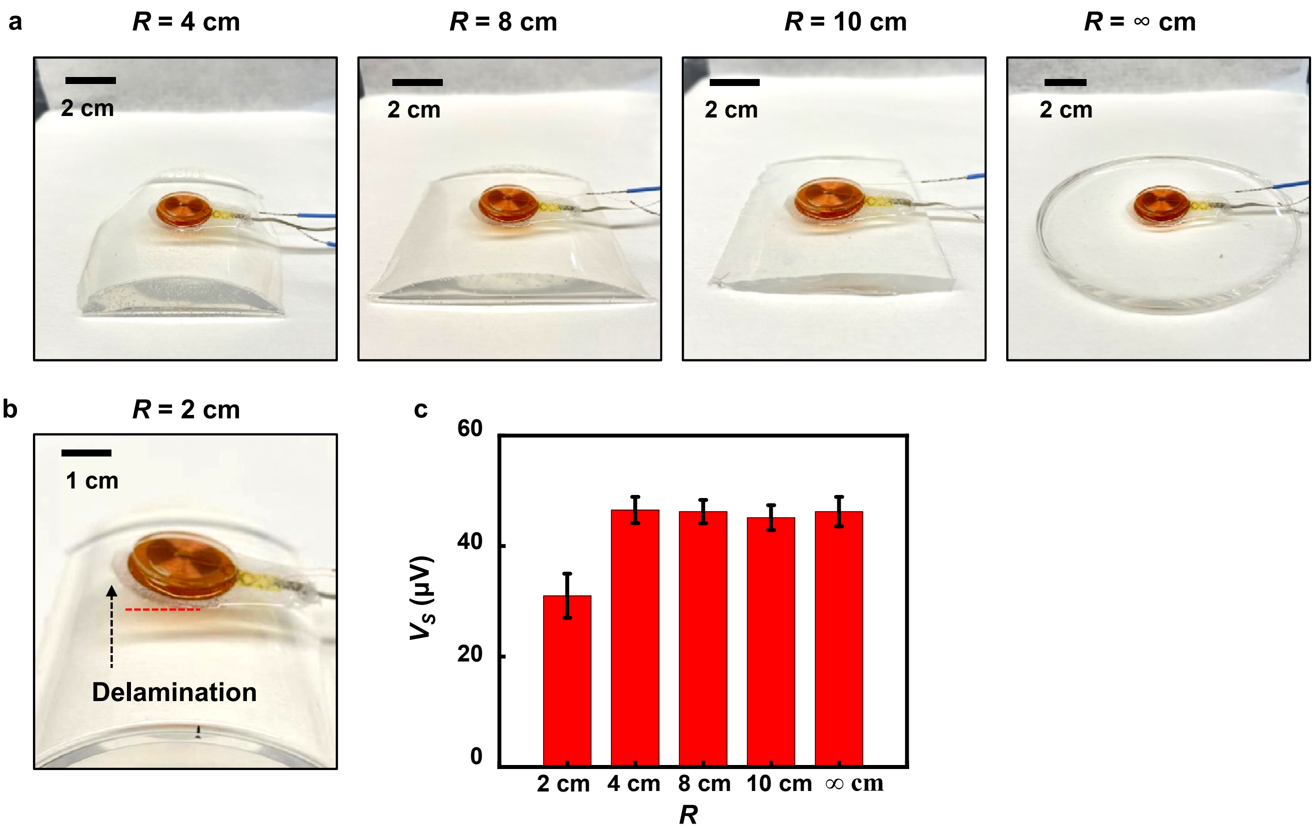

Figure S7. Systematic studies of the bending effects of EMM sensor measurements. (a) EMM sensors coupled on cylindrical substrates of PDMS with radius of curvature of 4 cm, 8 cm, 10 cm and ∞ cm, respectively. (b) EMM sensors coupled on substrates with overlarge curvature with bending radius of 2 cm. Delamination occurs at the contact surface. (c) Signals of EMM sensors with different bending radii. Error bars correspond to the standard deviation for five measurements with a given device.

Figure S8

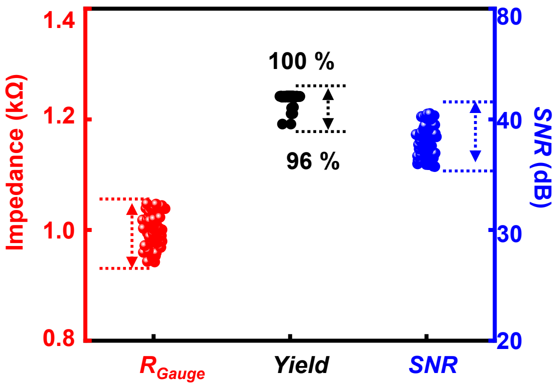

Figure S8. Statistics on the resistance (strain gauge), yield, and the *SNR* (during measurements on cheek) of 100 fabricated devices. The yield corresponds to the percentage of functional devices.

Figure S9

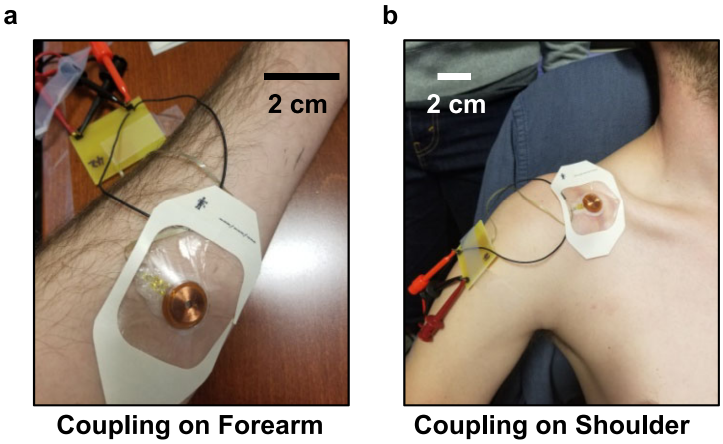

Figure S9. Applications of EMM sensors on human subjects. The system can be placed in contact with various locations of human body such as the (**a**) forearm and (**b**) shoulder. An adhesive film (3M Tegaderm Film) laminated on top of the entire structure prevents motion during measurements.

Figure S10

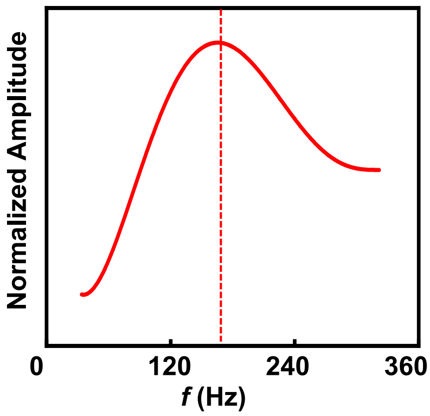

Figure S10. Normalized amplitude-frequency response of the vibratory actuator in contact with an artificial skin sample with an modulus of 200 kPa.

Figure S11

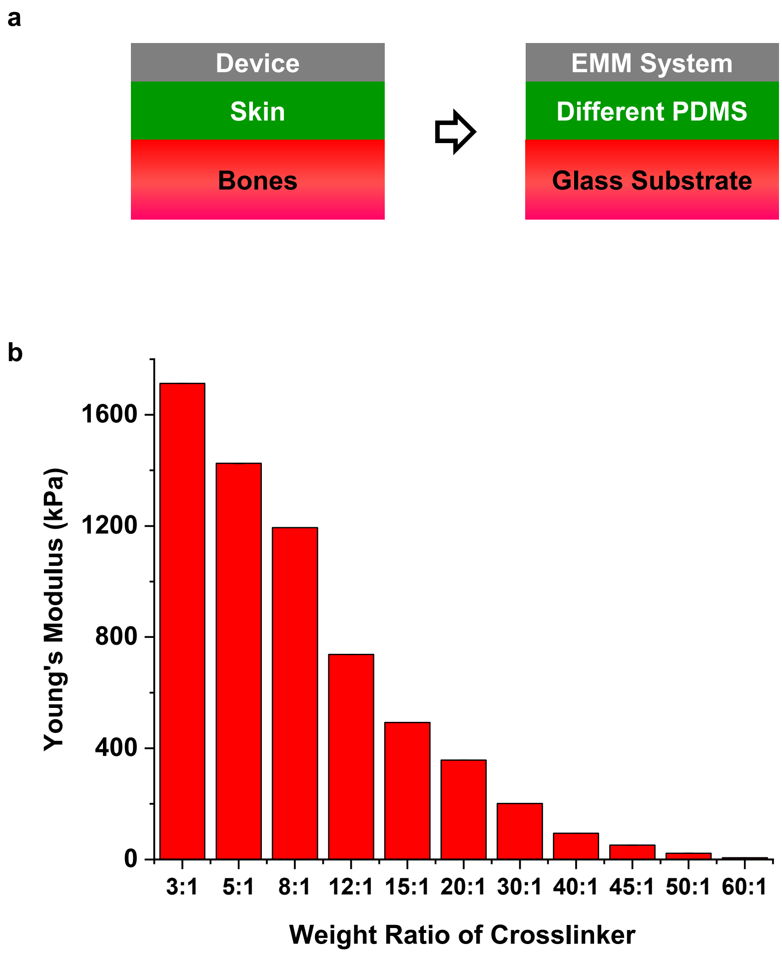

Figure S11. (**a**) Schematic diagram of an EMM sensor coupled onto artificial skin samples (PDMS layers) on glass substrates, as an approximate mimic of the structure of device/skin/bones. (**b**) A collection of measurements of elastic modulus on different PDMS layers, as function of weight ratios of crosslinker, all tested by the commercial bio-indenter.

Figure S12

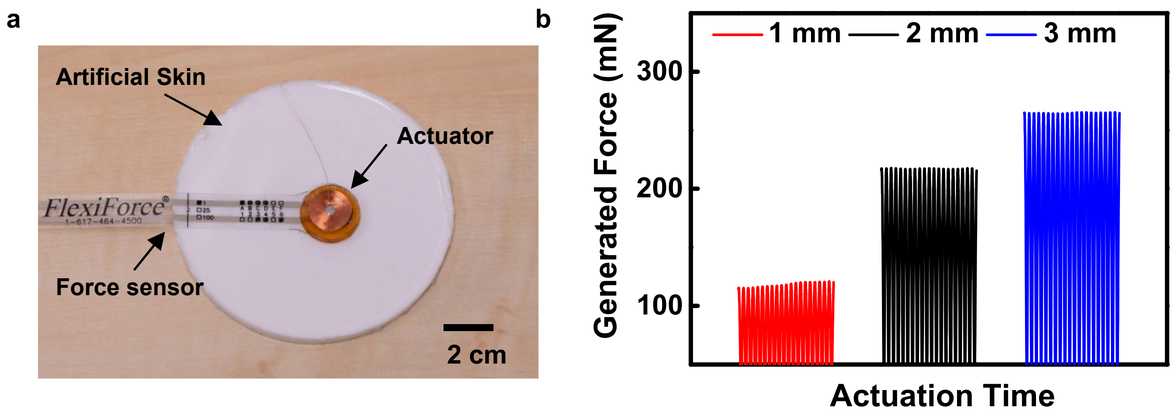

Figure S12. Measurements for force generated by the actuator. (**a**) Experimental setup for the force measurement, with a flexible force sensor placed between PDMS and actuator. (**b**, **c**, **d**) The generated force by magnet impact on (b) 1 mm-, (c) 2 mm- and (d) 3 mm-thick artificial skin (200 kPa).

Figure S13

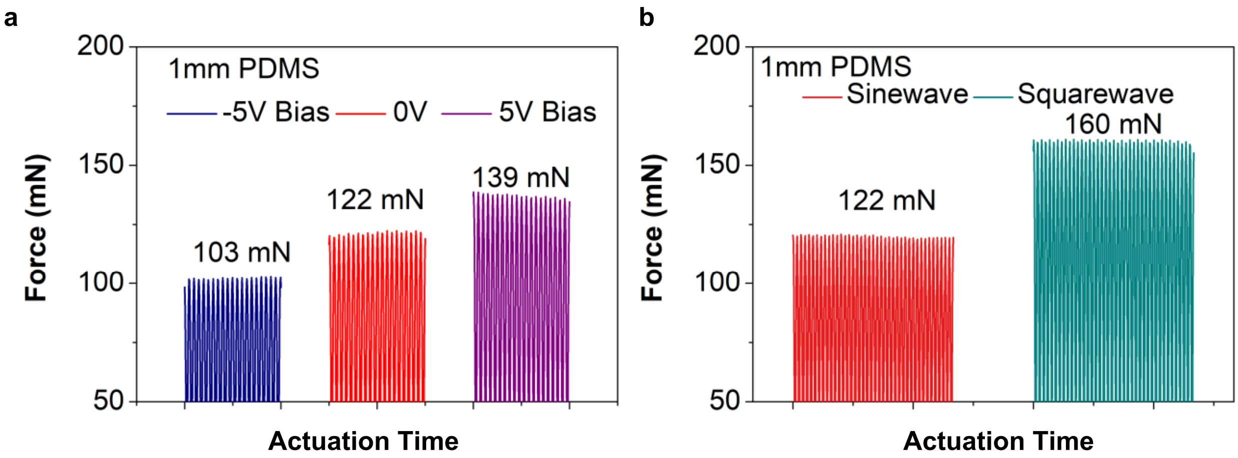

Figure S13. Strategies to increase the force on measurement targets. (a) Comparative results of the forces generated by applying different additional DC bias. (b) Generated force by sine-wave and square-wave input voltage with the same amplitude (5 V).

Figure S14

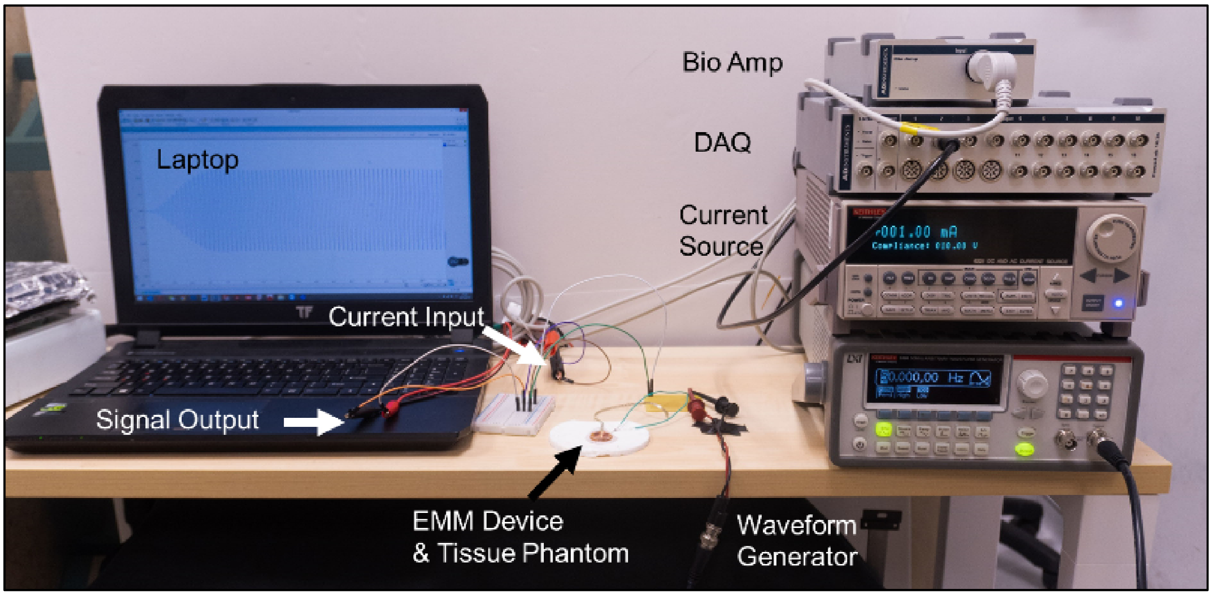

Figure S14. Photograph for the measurement setup to record the time signal of sensor.

Figure S15

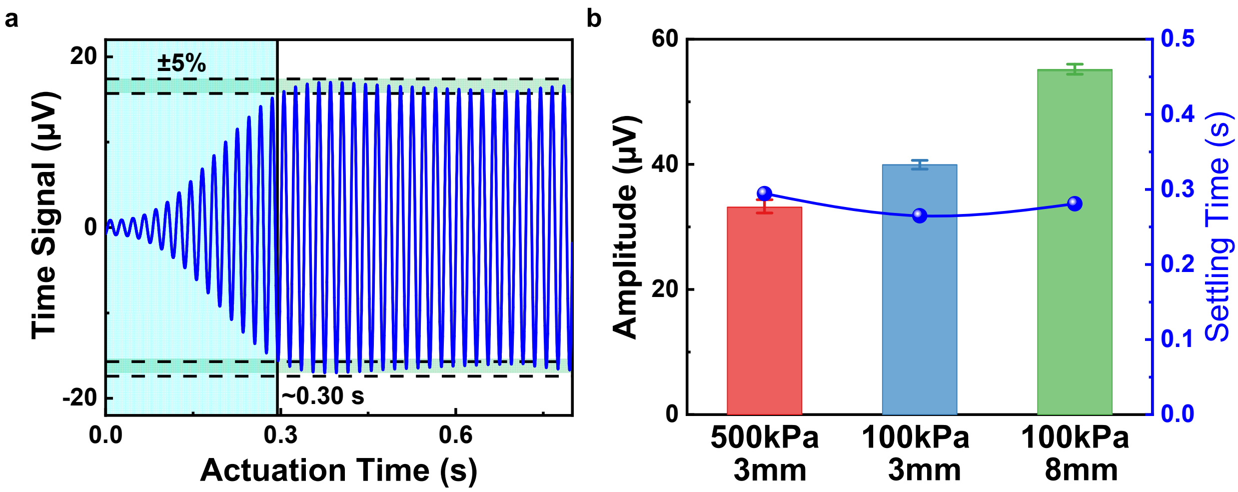

Figure S15. Time signals of sensor on different artificial skins. (**a**) Signal measured on tissue-phantom model (PDMS, 1mm thick, 500 kPa) as a function of actuation time, with amplitude variations < 5% and settling time of ~0.3 s. (**b**) Amplitudes of signal and settling time measured on different types of samples with various thicknesses and moduli, measured among 10 devices.

Figure S16

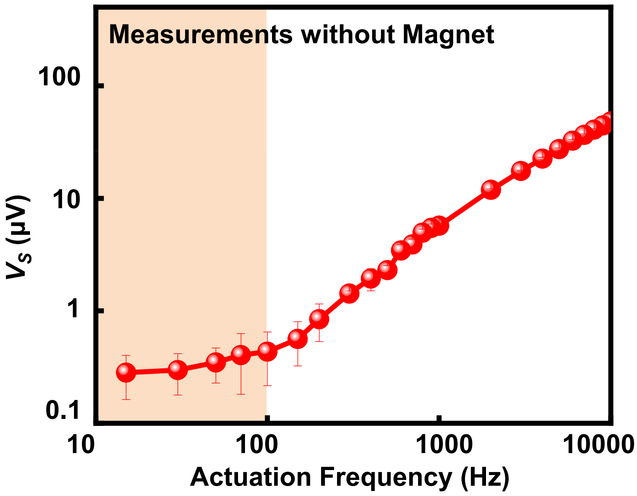

Figure S16. Recording of sensing voltages of V_S as function of actuation frequencies on artificial skin samples with elastic moduli of 200 kPa, without the magnets.

Figure S17

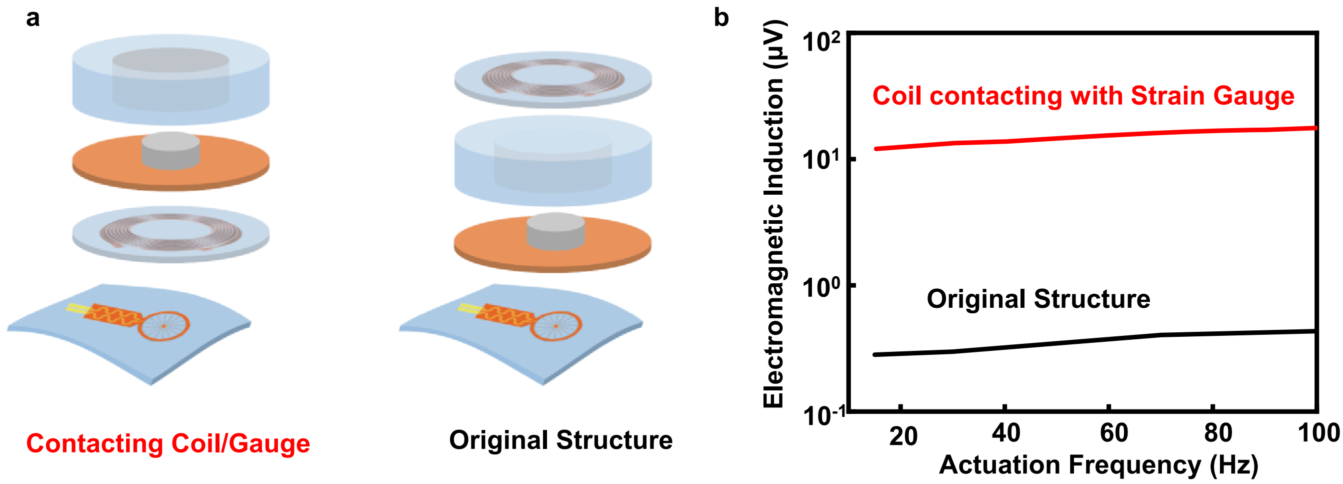

Figure S17. (**a**) Schematic illustration for two device structures, with coil contacting on strain gauge and the original construct in Fig. 1a. (**b**) Induced voltages by electromagnetic induction effect in EMM sensor as a function of actuation frequencies, in different designs.

Figure S18

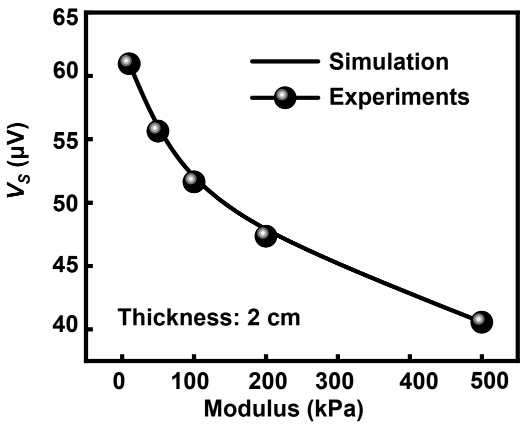

Figure S18. Simulated (line) and measured (symbols) V_S as a function of elastic modulus of the PDMS sample at 50 Hz, with constant thickness of 8 mm.

Figure S19

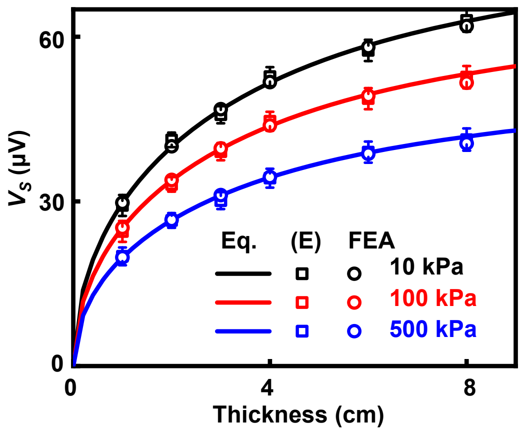

Figure S19. Results of experimental (E), FEA results and the fitting lines (Equation 1) of V_S as a function of sample thicknesses with various sample moduli.

Figure S20

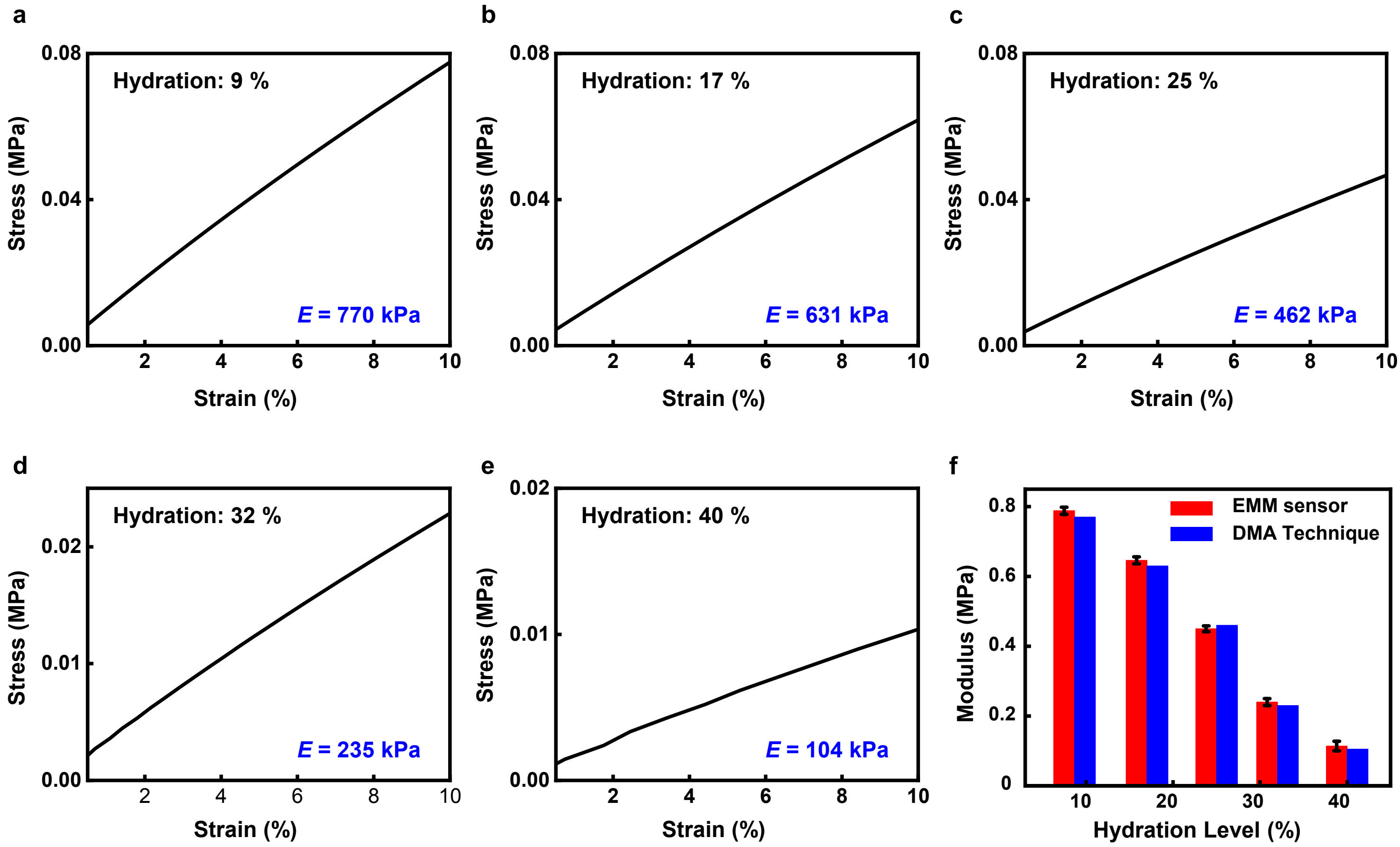

Figure S20. Mechanical evaluation of *ex-vivo* porcine skin via DMA techniques. (**a**)-(**e**) Stress-strain responses of the porcine skin with different hydration level tested by DMA in quasi-static strain rate regimes, with different modulus values. (**f**) Comparative modulus results from EMM sensor (red) and from DMA methods (blue).

Figure S21

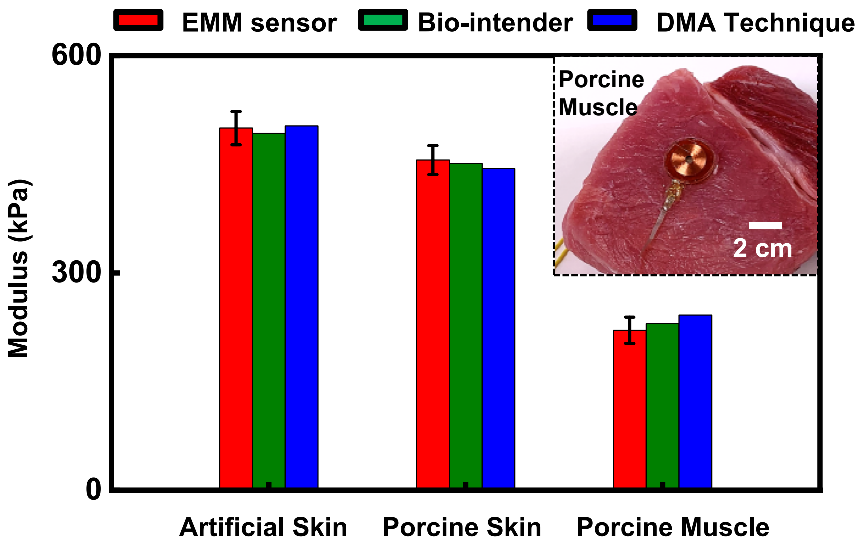

Figure S21. Summarized modulus measurements of tissue-phantom model, porcine skin and muscles via different methods, with inset of photograph of measurement on porcine muscle. Inset shows the photograph of measurement with EMM sensor on porcine muscle (5 cm thick).

Figure S22

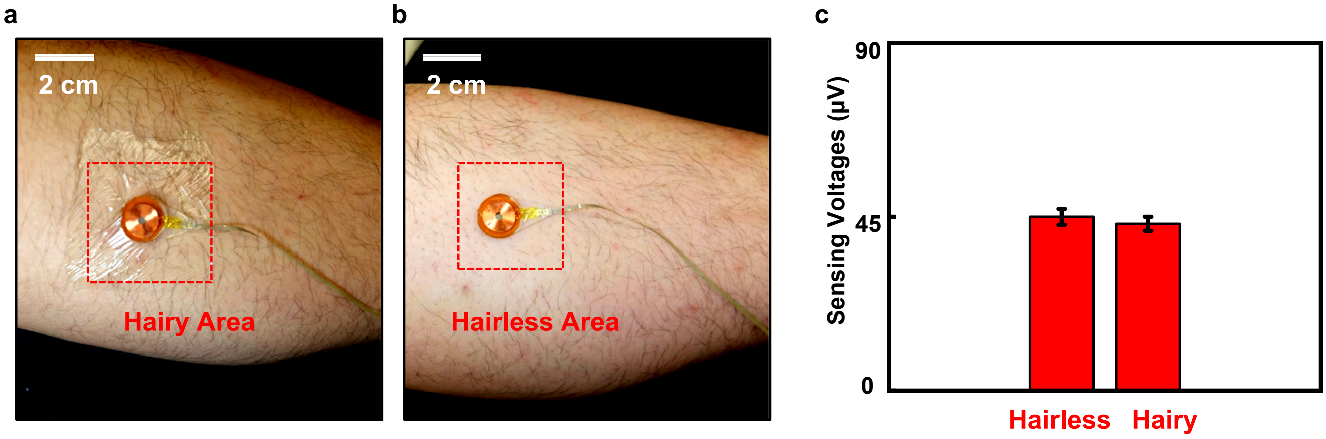

Figure S22. Comparison of measurement results with EMM sensors on the same location of a human thigh with (**a**) hair bearing and (**b**) hairless regions. (**c**) The output sensing voltages show stable performance on both regions.

Figure S23

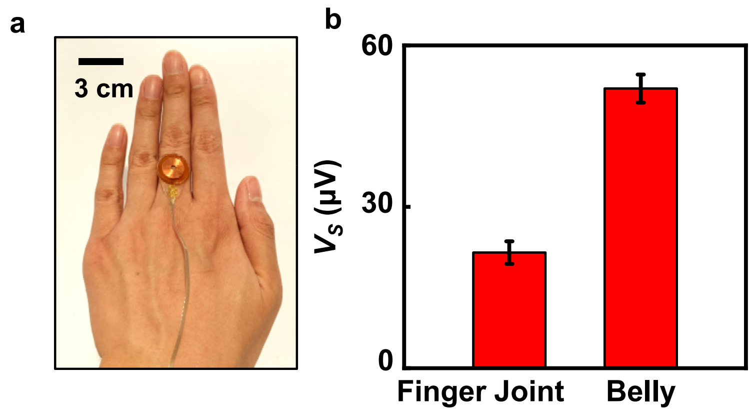

Figure S23. Measurement results at different body sites. (**a**) Photograph of measurement on finger joint. (**b**) Signals obtained at the sites in (a) and at belly region of a volunteer subject.

Figure S24

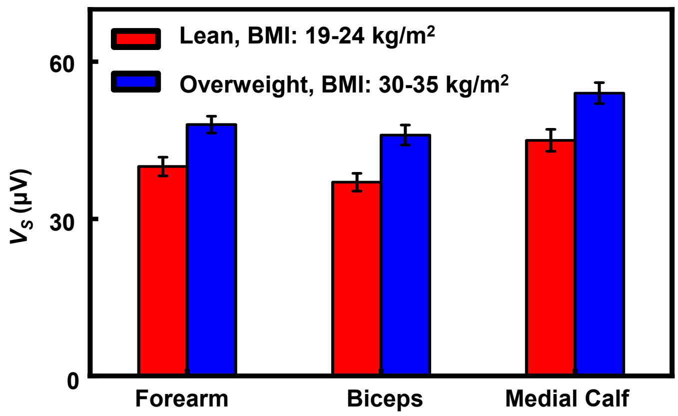

Figure S24. Comparative results of signals with device measurements on different locations of human body between lean subjects (red) and overweight (blue) subjects. To expand the signal variation, devices were mounted on test region with underlying muscle stressed during all measurements. Error bars correspond to the standard deviation for measurements among volunteer subjects.

Figure S25

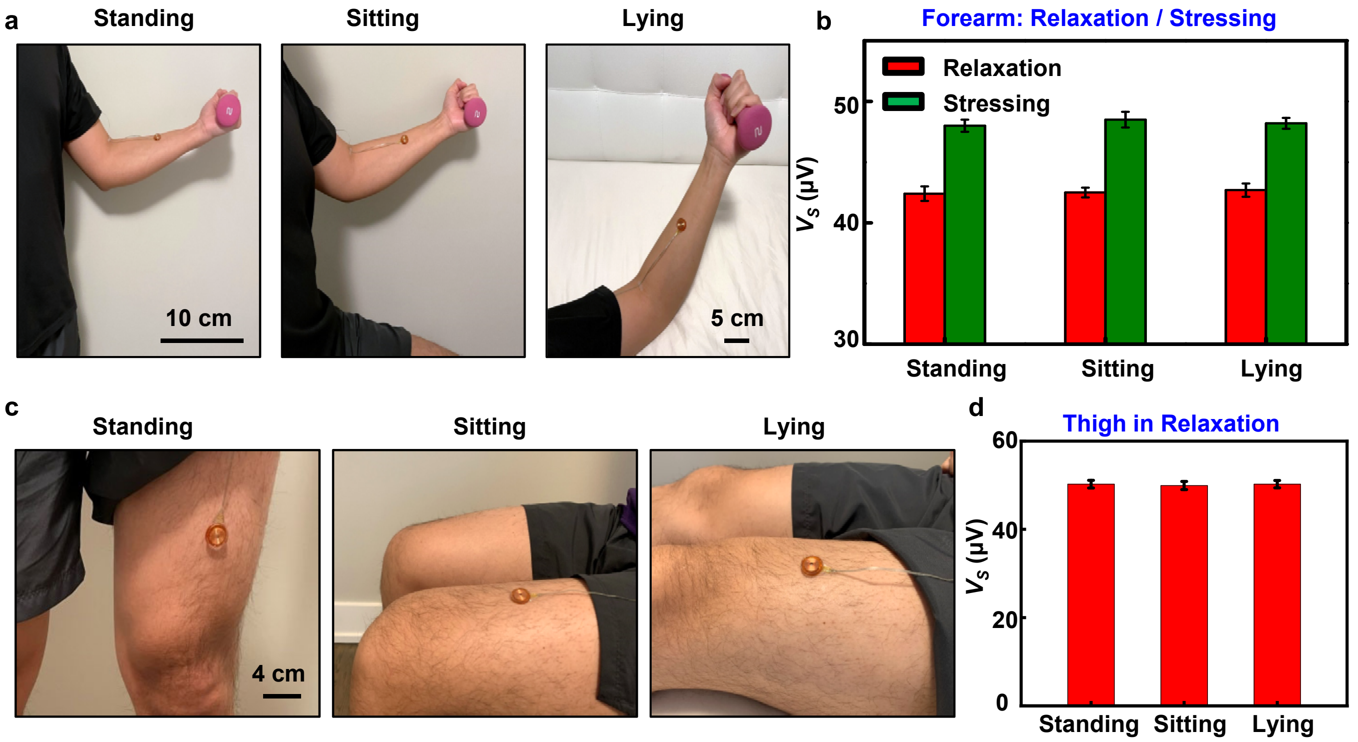

Figure S25. Measurements of various muscle states. (**a,b,c**) Photographs of devices coupled on thigh region of a volunteer subject during muscle states of (a) standing, (b) sitting and (c) lying (from left to right). (**d**) Measurement signals for different muscle states.

Figure S26

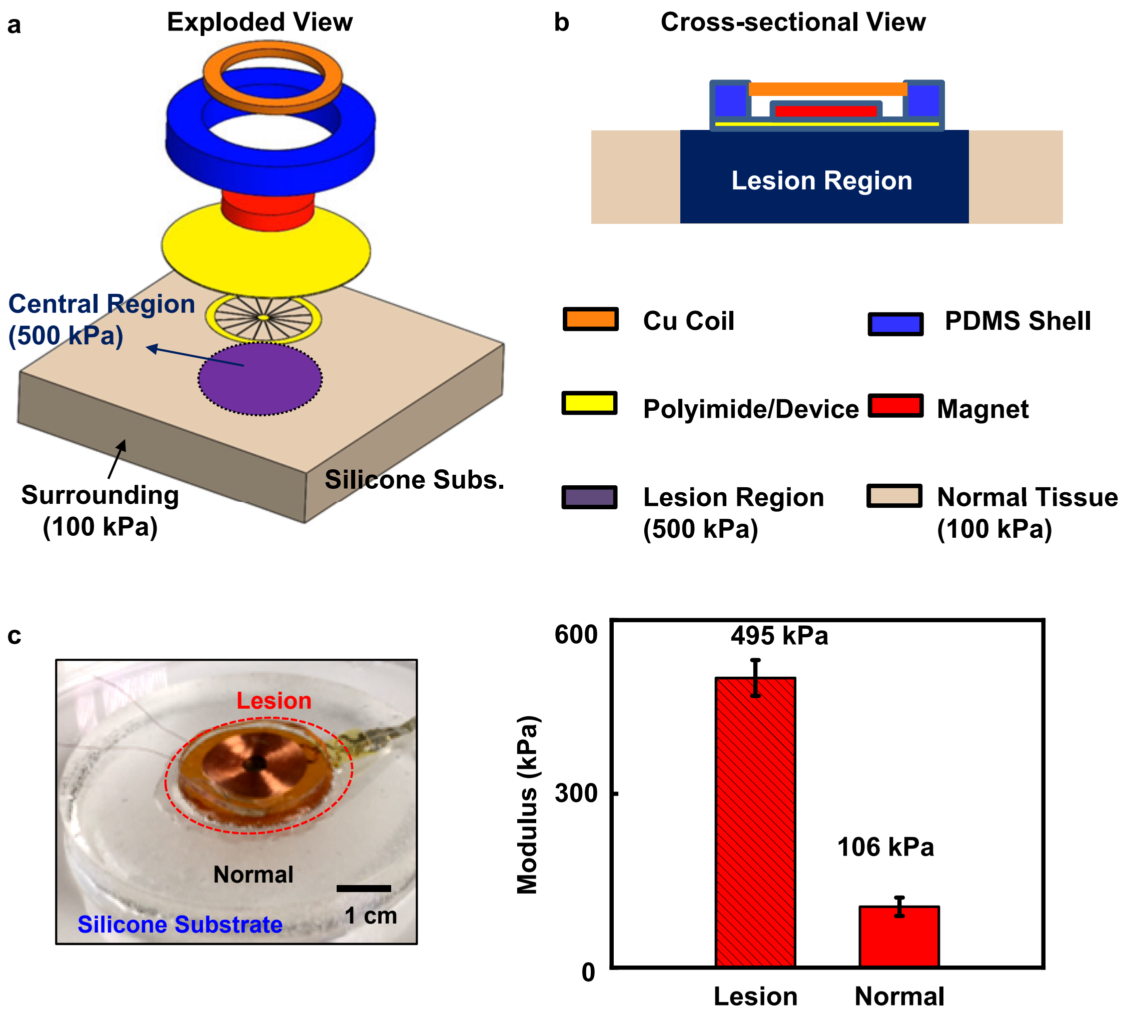

Figure S26. Schematic illustration of a simulated patient test. EMM sensors are coupled onto a silicone substrate (1 cm thick), with modulus of 500 kPa for the central part (1 cm diameter) and of 100 kPa for the surrounding part of the substrate that mimics the structure of a skin tumor, in an exploded (**a**) and cross-sectional (**b**) view. (**c**) Measurement results of the simulated patient test. Left: Photograph of the simulated test. Right: EMM measurements of modulus values at the central and surrounding regions of the silicone substrate.

Figure S27

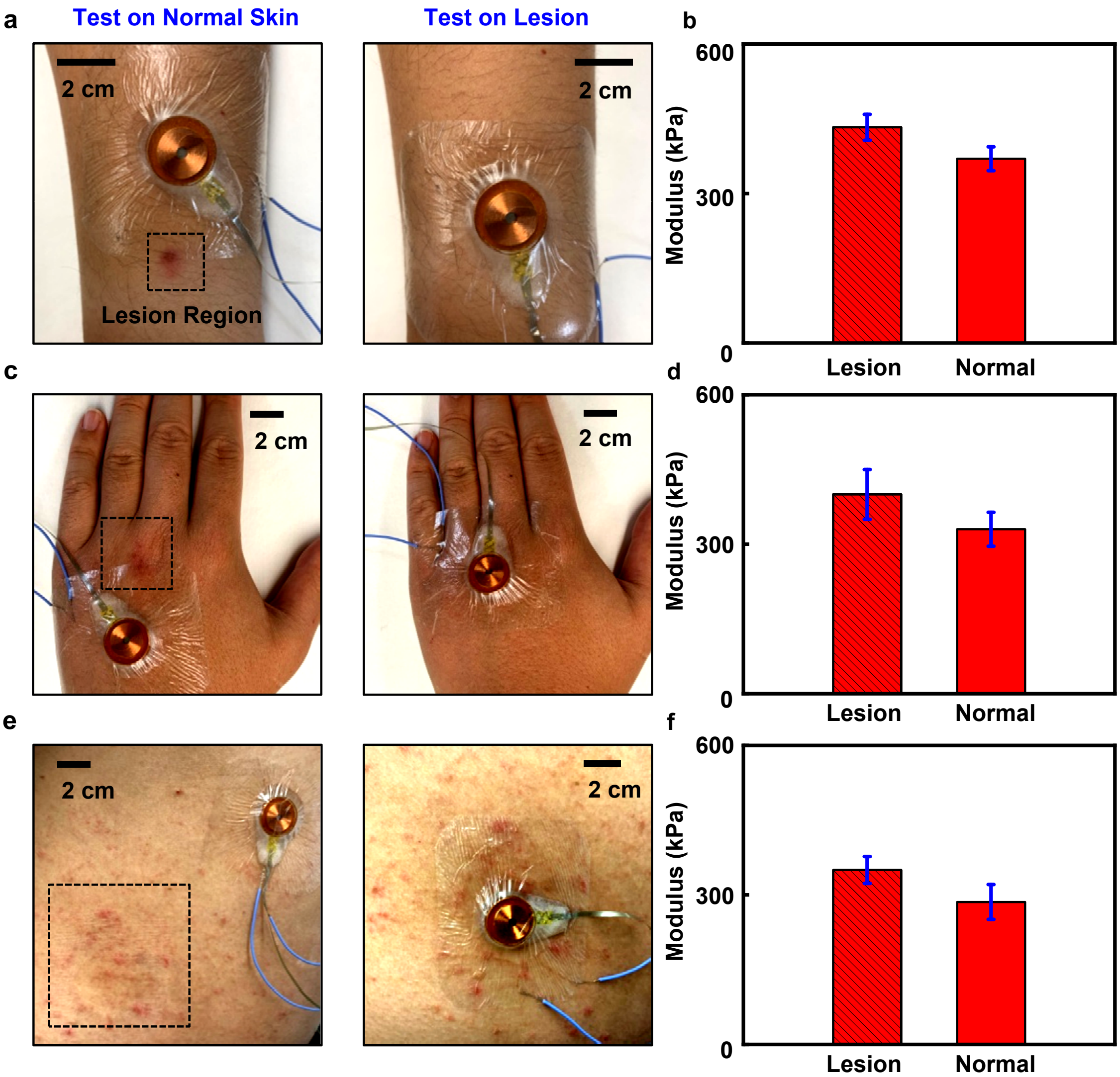

Figure S27. EMM measurements on (**a**) arm (**c**) hand and (**e**) lower back, with sensors on psoriasis lesion (right) and on nearby skin under normal conditions (left). Black frames correspond to the lesion regions of psoriasis. (**b**), (**d**), (**f**) Measurement results for the modulus values of lesions and nearby normal skin, collected in (**a**), (**c**) and (**e**). Error bars correspond to standard deviation for multiple measurements within a same subject.

Figure S28

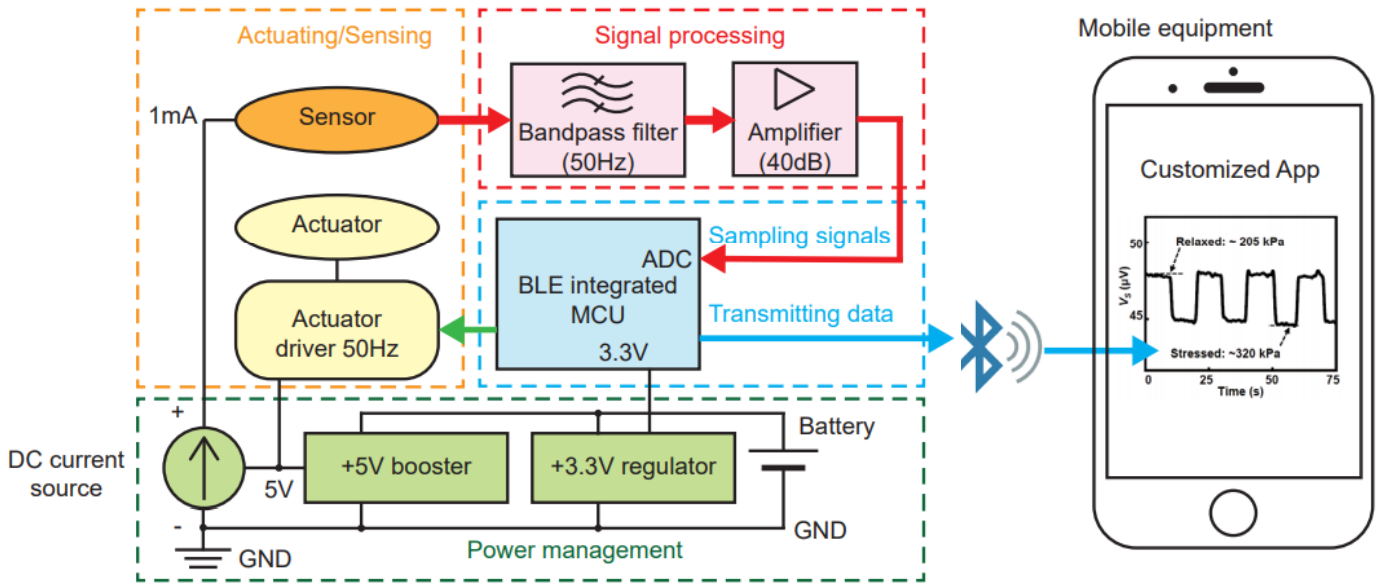

Figure S28. Schematic diagram of a feasible fully-wearable system under wireless control.

Figure S29

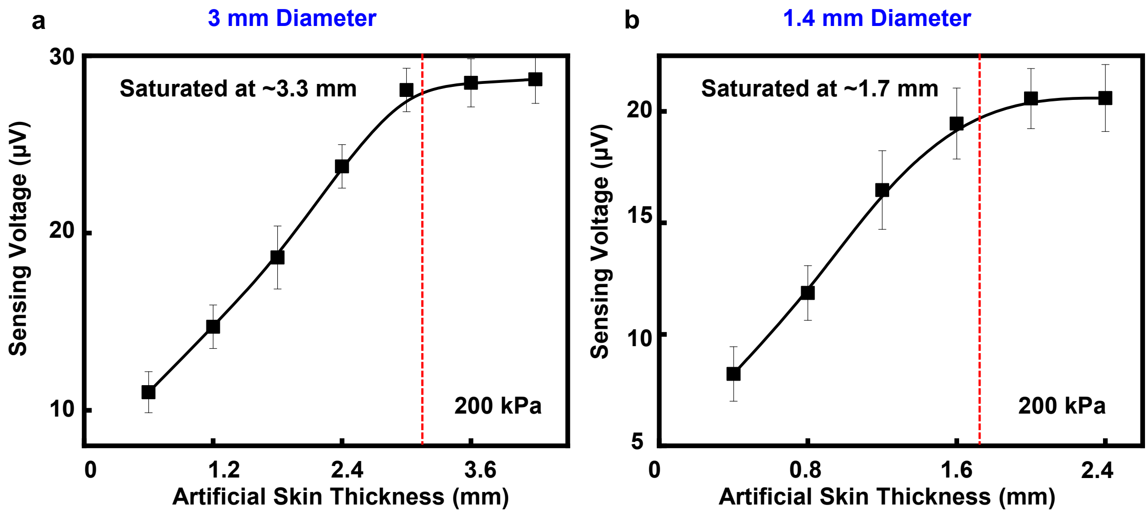

Figure S29. Experimental results for sensing voltages from EMM sensors with (**a**) 3 mm diameter and (**b**) 1.5 mm diameter magnets as function of the thickness of artificial skin samples.

Figure S30

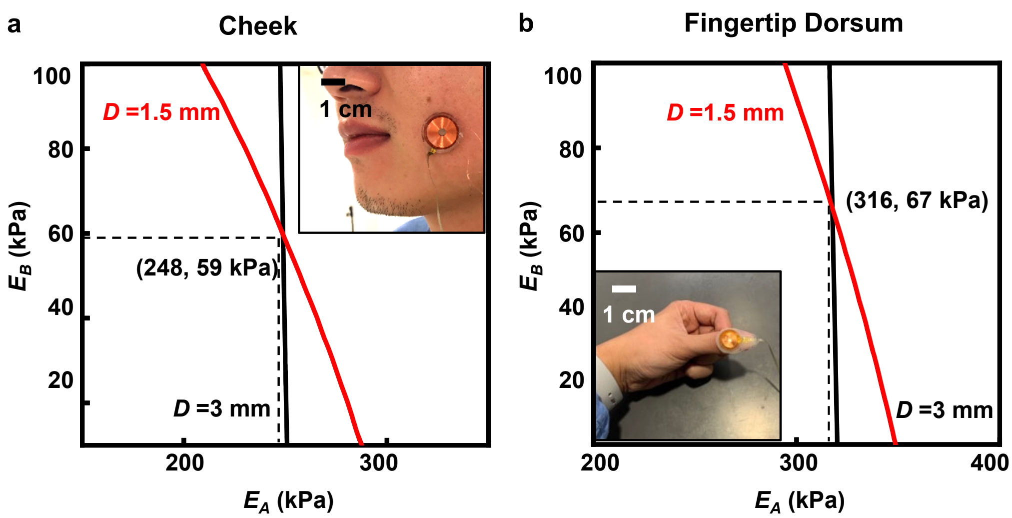

Figure S30. FEA modeling to determine the modulus of skin and inner tissues for (**a**) cheek region and (**b**) fingertip dorsum from measurements using EMM sensors with different D. Here, E_A and E_B correspond to elastic modulus for skin and inner tissues. Insets show the photographs of the measurements.

Figure S31

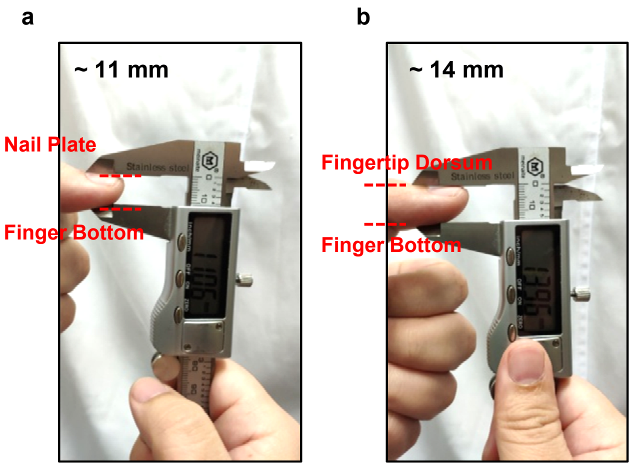

Figure S31. Simple estimation of tissue thickness in fingertip dorsum, with length measurements (**a**) from bottom of fingertip to nail plate; and (**b**) from bottom of fingertip to fingertip dorsum near the nail plate. The combined thickness for skin/tissues of fingertip dorsum near the nail root is ~3 mm.

Figure S32

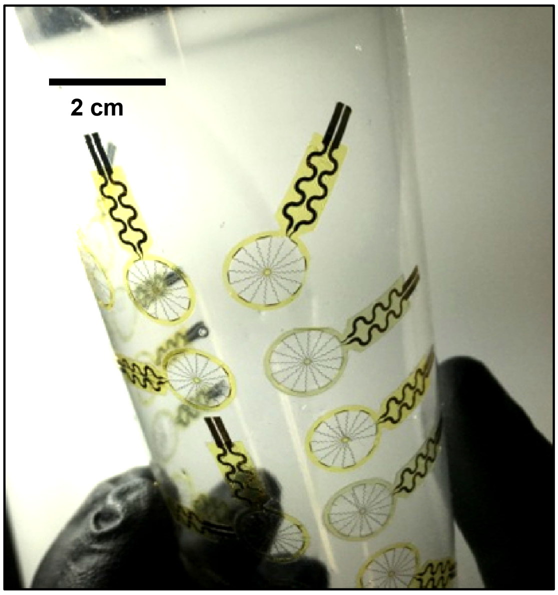

Figure S32. Photograph of the strain gauge array on a polymer substrate during bent status.

Figure S33

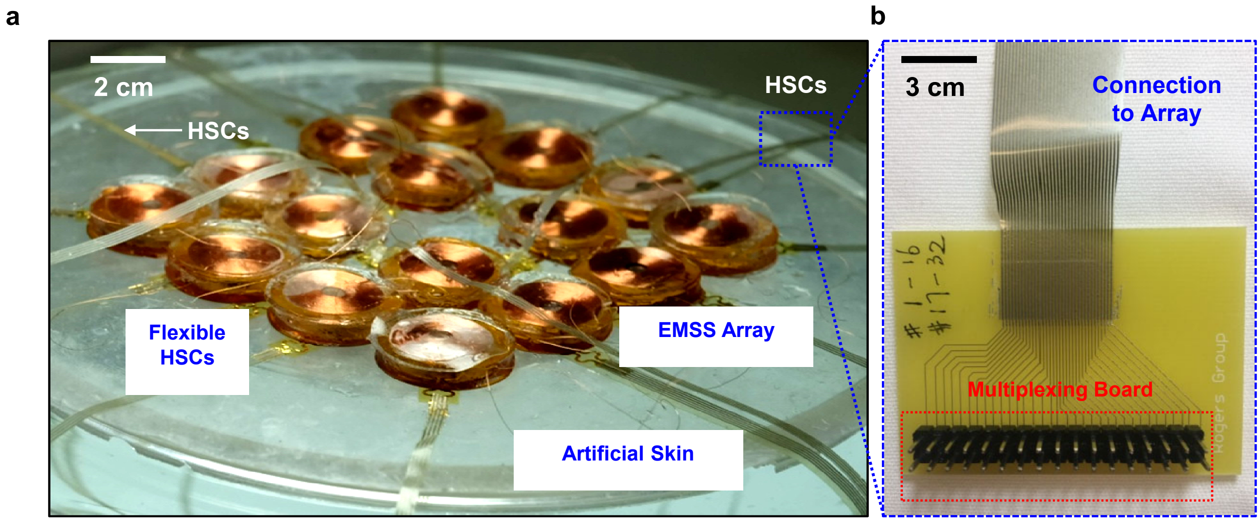

Figure S33. (**a**) Photograph of the final, complete EMM mapping array laminated on an artificial skin (PDMS, 2 cm thick). Interconnections use flexible cable of heat seal connectors (HSCs). (**b**) The connection of the EMM array system to an external multiplexing board.

Figure S34

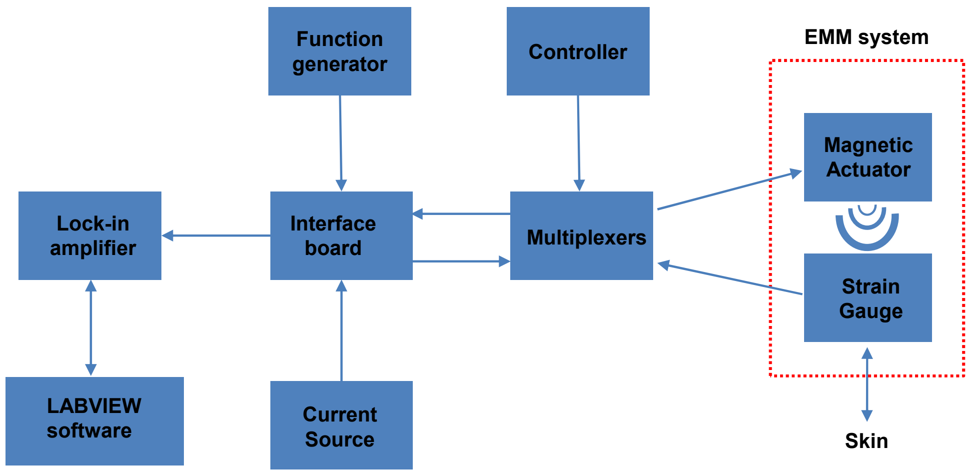

Figure S34. Schematic illustration of the DAQ system.

Table S1

E (kPa)	C(E)
10	1.53E-05
100	1.30E-05
500	1.02E-05

Table S1. The relationship between the elastic modulus E and $C(E)$ in Equation (1).

Table S2

Studies	Year	Lesion Types	Location	Lesion Modulus	Normal Modulus	Methods	Subject
Ref. 50	2006	Scleroderma	Finger	~450 kPa	~90 kPa	Ultrasound	Skin
Ref. 50	2007	Scleroderma	Hand	~150 kPa	~50 kPa	Ultrasound	Skin
Ref. 20	2015	Malignancy	Face	~6 MPa	~4.8 MPa	Piezoelectric	Skin
Ref. 51	2017	Edema	Chest Wall	69 ±4 kPa	63 ±6 kPa	Ultrasound	Skin
Ref. 51	2017	Scleroderma	/	~300 kPa	~80 kPa	Ultrasound	Skin
This Work	**/**	**Psoriasis**	**Back**	**~350 kPa**	**~281 kPa**	**EMM**	**Skin**
Ref. 52	2007	Fibroadenoma	Breast	6.41±2.86 kPa	~3.24 kPa	Indentation	Tissue
Ref. 21	2018	Tissue Tumor	Liver	~23 kPa	~10 kPa	Piezoelectric	Tissue
Ref. 21	2018	Tissue Tumor	Kidney	~40 kPa	~20 kPa	Piezoelectric	Tissue

Table S2. Summary of specific diseases and corresponding tissue mechanics. All values reported can be found in the corresponding references[20,21,50-52].